Journal of Sustainability for Energy
https://www.acadlore.com/journals/JSE

Improving Temperature Uniformity in Cylindrical Lithium-Ion Batteries Using Variable-Radius Annular Cooling Fins

Giulio Lorenzini[1*], Rasoul Fallahzadeh[1], Luca Cattani [1], Pamela Vocale [2], Rachele Schiasselloni[1], Darío Pavón-Vargas[1], Stefano Pollice [1]

[1] Department of Industrial Systems and Technologies Engineering, University of Parma, 43121 Parma, Italy
[2] Department of Engineering and Architecture, University of Parma, 43121 Parma, Italy

* Correspondence: Giulio Lorenzini (giulio.lorenzini@unipr.it)

Received: 07-18-2026 **Revised:** 09-09-2026 **Accepted:** 09-15-2026

Citation: G. Lorenzini, R. Fallahzadeh, L. Cattani, P. Vocale, R. Schiasselloni, D. Pavón-Vargas, and S. Pollice, "Improving temperature uniformity in cylindrical lithium-ion batteries using variable-radius annular cooling fins," *J. Sustain. Energy*, vol. 5, no. 3, pp. 248–259, 2026. https://doi.org/10.56578/jse050305.

© 2026 by the author(s). Published by Acadlore Publishing Services Limited, Hong Kong. This article is available for free download and can be reused and cited, provided that the original published version is credited, under the CC BY 4.0 license.

Abstract: Effective thermal management is essential for the reliable operation of lithium-ion batteries (LIBs) in electric vehicles (EVs) and other energy storage applications. In cylindrical cells, anisotropic thermal conductivity makes it difficult to maintain a uniform internal temperature, particularly under air-cooling conditions. This study investigates the effects of annular cooling fins with different radius distributions on the thermal performance and internal temperature uniformity of a cylindrical LIB. A three-dimensional transient electrochemical–thermal model was developed in COMSOL Multiphysics, coupling a one-dimensional pseudo-two-dimensional (P2D) electrochemical model with heat transfer and airflow simulations. Five annular fin configurations were evaluated against a finless design under forced-air cooling conditions. The numerical model was validated against published experimental measurements of cell voltage and surface temperature. The results showed that all fin configurations reduced the maximum cell temperature and internal temperature difference compared with the finless design. The uniform-radius configuration produced the lowest maximum temperature, whereas the increasing-radius configuration achieved the most uniform internal temperature distribution. Compared with the uniform-radius configuration, the increasing-radius design reduced the average maximum intra-cell temperature difference by 5.8%, fin material consumption by 37.5%, and airflow pressure drop by approximately 15%. These findings indicate that the distribution of annular fin radii plays an important role in balancing heat dissipation, internal temperature uniformity, and aerodynamic resistance. The study provides a practical basis for the design of air-cooled thermal management systems for cylindrical LIBs.

Keywords: Lithium-ion batteries; Battery thermal management; Temperature uniformity; Annular cooling fins; Electrochemical–thermal modeling; Air cooling

1 Introduction

The growing adoption of electric vehicles (EVs) has increased the demand for reliable energy storage systems, with lithium-ion batteries (LIBs) becoming a widely used option [1] due to their high energy density [2]. However, battery performance, operational safety, and service life are strongly influenced by temperature. The maximum operating temperature of LIBs is commonly limited to 60 °C [3], while the preferred operating range is generally between 20 °C and 40 °C [4]. In addition to maintaining a suitable operating temperature, temperature differences between cells in a battery module should remain below 5 °C [5] to support long-term battery operation [6] and maintain electrical balance among individual cells [7]. Temperature uniformity is equally important within each cell [8]. Internal temperature gradients can generate thermal stresses and accelerate degradation, contributing to capacity loss, increased internal resistance, and self-discharge [9]. Effective battery thermal management must therefore address both the overall operating temperature and its spatial distribution.

Air cooling is widely used in battery thermal management systems (BTMSs) because of its relatively simple construction, low maintenance requirements, absence of liquid leakage risks, and generally modest auxiliary energy demand [8]. Cylindrical LIBs, which are commonly employed in EV battery systems [10], present particular challenges for air-based thermal management. Their spirally wound electrode assemblies form a layered structure

with anisotropic thermal conductivity. Heat conduction is relatively effective in the axial and circumferential directions but considerably weaker in the radial direction. Nevertheless, cooling is commonly applied through the curved outer surface rather than the terminal surfaces because of the larger available heat transfer area [11]. This arrangement creates a need for cooling structures that can remove heat effectively while limiting temperature differences within the cell.

The relatively low convective heat transfer coefficient of air restricts the cooling capacity of conventional air-based BTMSs. Attaching fins directly to the surfaces of cylindrical cells offers a means of increasing the heat transfer area and modifying the surrounding airflow [12]. Although fin-assisted cooling has been investigated extensively for prismatic and pouch cells, comparatively fewer studies have examined fins mounted directly on cylindrical LIBs. Existing research on cylindrical cells has mainly considered longitudinal, spiral, and annular fin geometries, with particular attention to maximum temperature reduction and temperature differences between cells.

Among the earlier investigations, Öztop and Şahinaslan [13] used computational fluid dynamics (CFD) to examine an air-cooled module containing 24 cylindrical 18650 cells, comparing configurations with and without longitudinal fins. Their results showed that the fins improved heat dissipation and reduced both the maximum cell temperature and the maximum temperature difference between cells. Shehabaz et al. [14] subsequently investigated a single cylindrical 21700 cell using a combined CFD and response surface methodology (RSM) approach. They reported that longitudinal fins provided additional cooling beyond forced convection alone, primarily through the increased heat transfer area and changes in the thermal boundary layer and local airflow. Alfred Francis et al. [15] examined conventional and tapered longitudinal fins for an air-cooled 21700 cell. Their simulations indicated that tapering did not substantially alter cooling performance under the relatively uniform airflow conditions considered. Together, these studies show that the cooling performance of longitudinal fins depends not only on their surface area but also on their interaction with the surrounding flow.

Alternative fin geometries have been investigated to modify airflow around cylindrical cells. Alzwayi and Paul [16] compared spiral and longitudinal fins for a single cylindrical 21700 cell using CFD simulations. The spiral geometry redirected the airflow around the cell, increasing flow mixing and improving heat removal. In a subsequent investigation [9], the same authors extended the comparison to a module containing 15 cylindrical 21700 cells. Spiral fins reduced the maximum temperature and inter-cell temperature differences more effectively than longitudinal fins or a finless arrangement. The improvement was associated with stronger airflow circulation within the cooling channel, although the additional flow mixing also increased the pressure drop. Alfred Francis et al. [15] further reported that the axial extension and tapering of spiral fins could improve fin effectiveness, particularly when the fin surface area was distributed in regions with relatively small temperature gradients. These findings indicate that fin geometry and its spatial distribution influence both thermal performance and aerodynamic resistance.

Annular fins provide another approach to controlling heat transfer from cylindrical batteries. Chaudhari et al. [17] investigated annular fins attached to the outer surfaces of 16 cylindrical 18650 cells and reported reductions in the maximum temperature and maximum inter-cell temperature difference. To accommodate the limited space available in air-cooled battery systems, Han et al. [18] proposed slotted annular fins that allowed a greater fin extension and heat transfer area. Their design reduced the average cell temperature compared with conventional annular fins, although temperature differences remained between cells at different positions in the module. The authors subsequently introduced unequal-length slotted fins to address this variation. Longer fins were assigned to cells operating at higher temperatures to increase heat dissipation, while shorter fins were used for cooler cells to avoid excessive cooling. This arrangement demonstrated the importance of distributing the cooling surface according to local thermal conditions.

A direct comparison of longitudinal, spiral, and annular fins was presented by Omar and Adham [19] using CFD simulations of a single cylindrical 21700 cell. All three geometries reduced the maximum temperature and improved the temperature distribution relative to the finless cell. Among the configurations examined, annular fins produced the most favorable thermal performance, which was attributed to the distribution of airflow around the battery surface. These results suggest that annular fins are a suitable candidate for further investigation, particularly when the arrangement and dimensions of individual fins can be varied along the cell.

Despite these developments, most studies of fin-assisted cylindrical battery cooling have concentrated on the maximum cell temperature or the temperature difference between cells within a module. The investigation by Shehabaz et al. [14] also considered temperature variation within an individual cell, but the influence of annular fin geometry on the maximum intra-cell temperature difference remains less thoroughly examined. Although annular fins have shown favorable cooling performance in comparisons with other geometries [19], a reduction in maximum temperature does not necessarily correspond to the most uniform internal temperature distribution. Moreover, the distribution of fin radii may alter local heat transfer and airflow resistance, making it important to examine these effects together. A further consideration is the representation of heat generation within the battery. Previous fin-cooling studies have commonly prescribed heat generation as a constant or time-dependent input, whereas coupling electrochemical heat generation with the evolving thermal field allows the interaction between battery operation and

cooling conditions to be represented more directly.

To address these issues, this study investigates the effects of annular cooling fins with uniform and variable radii on the internal temperature uniformity of a single cylindrical LIB. A three-dimensional transient electrochemical–thermal model was developed by coupling a one-dimensional pseudo-two-dimensional (P2D) electrochemical model with three-dimensional heat transfer and airflow simulations. Five annular fin configurations were compared with a finless design under the same forced-air cooling conditions. The analysis considers the maximum cell temperature, maximum intra-cell temperature difference, airflow distribution, and pressure drop, with particular attention to the relationship between fin radius distribution and thermal uniformity. The numerical model was also evaluated against published experimental measurements of cell voltage and surface temperature. By examining internal temperature uniformity alongside heat dissipation and aerodynamic resistance, the study provides a basis for selecting annular fin arrangements for air-cooled cylindrical LIBs used in EVs and related energy storage applications.

2 Numerical Methodology

A three-dimensional transient electrochemical–thermal model was developed in COMSOL Multiphysics 6.2 to examine the influence of annular fin geometry on heat dissipation and internal temperature uniformity in a cylindrical LIB. The model coupled electrochemical heat generation with heat transfer in the battery and airflow through the cooling channel, allowing the thermal response to be evaluated under the prescribed discharge conditions. The simulations were performed on a computer equipped with an Intel Core i7-10610U processor and 16 GB RAM. The following subsections describe the computational geometry, governing equations, material properties, boundary conditions, numerical discretization, and validation against experimental measurements.

2.1 Geometry Description

The computational model was based on a cylindrical 18650 lithium-ion cell, a configuration widely used in EV applications [20]. The Panasonic NCR18650BD cell was selected as the reference battery. Its geometry and principal specifications are presented in Figure 1 and Table 1, respectively. The cell has a diameter of 18.25 mm, a height of 65.10 mm, and a rated capacity of 2.98 Ah. Its electrode materials consist of a nickel cobalt aluminum oxide cathode and a graphite anode, with the electrolyte and operating voltage limits specified in Table 1.

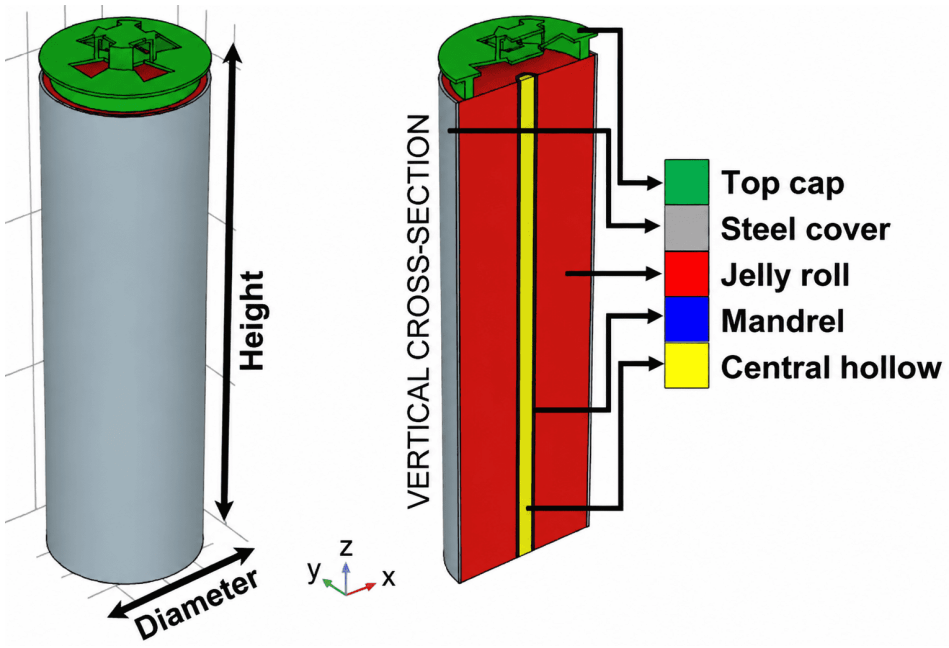


Figure 1. Computational geometry and constituent domains of the cylindrical lithium-ion cell

To represent the thermal characteristics of the cell, the geometry was divided into five domains: the steel cover, mandrel, central hollow region, top cap, and jelly roll, as illustrated in Figure 1. The dimensions, materials, and thermophysical properties assigned to these domains are listed in Table 2 [21–23]. The jelly roll, consisting of the positive electrode, separator, negative electrode, and current collectors, was represented as a homogenized active-material domain. Its anisotropic thermal conductivity was retained, with a radial conductivity of 0.413 W/(m·K) and axial and circumferential conductivities of 1.78 W/(m·K). This representation accounts for the directional heat conduction associated with the layered structure of the cylindrical cell.

Table 1. Main specifications of the Panasonic NCR18650BD cylindrical lithium-ion cell [21, 22]

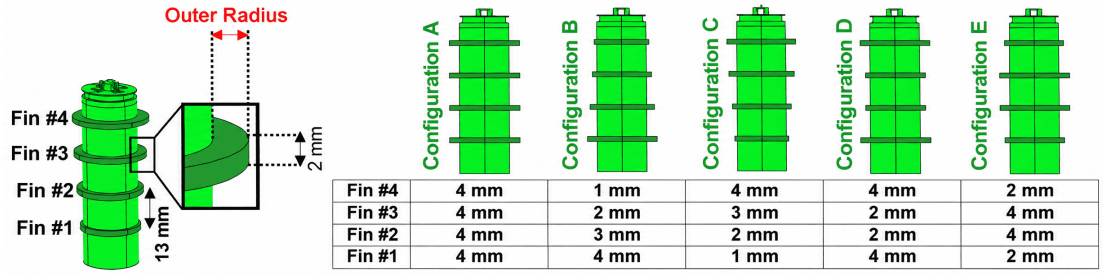
Items and Units	Value
Diameter [mm]	18.25
Height [mm]	65.10
Rated capacity [Ah]	2.98
Electrolyte material	Lithium salt ($LiPF_6$) in ethylene carbonate: ethyl methyl carbonate (1:1 by volume)
Cathode material	NCA: nickel cobalt aluminum oxide
Anode material	Graphite
Maximum charge voltage [V]	4.2
Minimum discharge voltage [V]	2.5

Table 2. Geometrical dimensions, materials, and thermophysical properties of the battery domains [21–23]

Items and Units	Value				
	Steel Cover	Mandrel	Central Hollow	Top Cap	Jelly Roll
Material	Steel	Steel	Air	Steel	Active material*
Height [mm]	60	60	60	5.10**	60
Outer diameter [mm]	18.25	2.5	1.75**	18.25**	17.5
Inner diameter [mm]	17.5	1.75**	—	13.75**	2.5
Density [kg/m^3]	8030	8030	1.225	8030	1113
Specific heat capacity [J/(kg·K)]	503	503	1006	503	959
Thermal conductivity [W/(m·K)]	16.27	16.27	0.0242	16.27	$k_r = 0.413$; $k_\theta = k_z = 1.78$

Note: "*" = the jelly roll, comprising the positive electrode, separator, negative electrode, and current collectors, was modeled as a homogenized domain referred to as the "active material"; "**" = the indicated values were estimated from the properties of the constituent components; "—" = not applicable.

Five annular fin configurations were considered in addition to the finless reference design, as shown in Figure 2. All fins were made of steel. Configuration A employed annular fins of uniform radius, whereas Configurations B–E used different distributions of fin radii along the cell. The individual fin dimensions and their arrangement are provided in Figure 2. These configurations were used to examine how the axial distribution of cooling surface area affects the maximum cell temperature and temperature uniformity within the jelly roll.



	Configuration A	Configuration B	Configuration C	Configuration D	Configuration E
Fin #4	4 mm	1 mm	4 mm	4 mm	2 mm
Fin #3	4 mm	2 mm	3 mm	2 mm	4 mm
Fin #2	4 mm	3 mm	2 mm	2 mm	4 mm
Fin #1	4 mm	4 mm	1 mm	4 mm	2 mm

Figure 2. Annular fin configurations with uniform and variable radii

The battery and fins were placed inside a Z-shaped rectangular cooling duct, as illustrated in Figure 3. Cooling air entered from the left side of the duct and exited from the right side. The same duct geometry was used for all configurations, allowing differences in thermal performance and airflow resistance to be attributed to the fin arrangements under otherwise identical operating conditions.

2.2 Model Development

The electrochemical and thermal responses of a LIB are closely coupled. Electrochemical reactions and internal resistance generate heat during discharge, while changes in temperature affect reaction kinetics and ion transport through temperature-dependent material properties. To account for this interaction, a P2D electrochemical model [24] was coupled with a three-dimensional transient thermal model. The electrochemical model calculated the heat

generated during discharge, which was supplied to the thermal model as a volumetric heat source. The resulting temperature field was then used to update the temperature-dependent parameters of the electrochemical model. This two-way coupling represented the interaction between electrochemical heat generation and heat removal by the surrounding airflow.

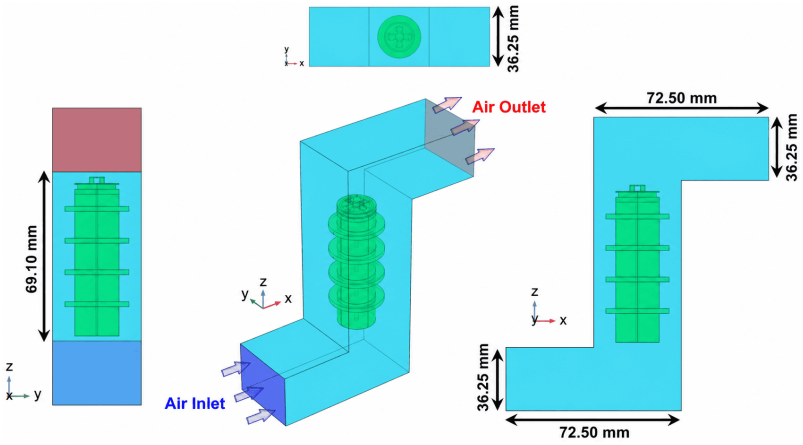


Figure 3. Geometry of the Z-shaped air-cooling channel

During discharge, electrons travel through the external circuit from the negative electrode toward the positive electrode, while lithium ions migrate through the electrolyte in the same overall direction. The separator prevents electronic conduction between the electrodes while permitting ionic transport. Charge conservation links the electronic and ionic currents, and the electrochemical model therefore includes charge conservation, species transport, and interfacial reaction kinetics.

Charge transport in the solid phase was described using Ohm's law, while ionic conduction in the electrolyte was represented using concentrated-solution theory. Lithium transport within the active-material particles was governed by Fick's second law in spherical coordinates, and electrolyte concentration changes were described by the corresponding species conservation equation. The intercalation and deintercalation reactions at the electrode–electrolyte interfaces were modeled using Butler–Volmer kinetics [25], which relates the interfacial reaction current density to the local overpotential and electrochemical conditions.

Heat generation during discharge was divided into three contributions: reaction heat (Q_{rea}), activation polarization heat (Q_{act}), and ohmic heat (Q_{ohm}). Their combined contribution provided the heat source for the thermal calculation. The electrochemical model adopted the following assumptions [26]: side reactions were excluded; active-material particles were represented as homogeneous spheres; electrode volume changes were neglected; and phase changes and gas formation were not considered. These assumptions defined the electrochemical processes included in the coupled simulation.

The governing equations and boundary conditions for charge conservation, mass conservation, electrochemical kinetics, and heat generation are summarized in Table 3 [25–27]. The corresponding parameter definitions and numerical values are provided in Table A1 of Appendix.

The heat generated by the electrochemical model was transferred to the three-dimensional thermal domain, where conduction within the battery and fins was coupled with convection in the cooling air. Temperature and velocity fields were calculated using the Heat Transfer in Solids and Fluids and Laminar Flow interfaces in COMSOL, coupled through the Nonisothermal Flow multiphysics interface. The thermal model accounted for transient heat transfer in the solid and fluid domains, while airflow was described by the Navier–Stokes and continuity equations. The governing equations are presented in Table 4 [28], with the relevant material properties listed in Table 2.

The cooling air entered the duct at a prescribed velocity of 0.25 m/s, corresponding to a Reynolds number of 521. Under these conditions, the airflow was modeled as laminar, Newtonian, and incompressible, with body forces neglected. The inlet air temperature was maintained at 25 °C, and atmospheric pressure was imposed at the outlet. The initial temperature of both the battery and the cooling air was set to 25 °C.

The thermal model assumed that the battery was the only heat-generating component and that the thermophysical properties of the airflow remained constant under the prescribed operating conditions. Heat generation within the jelly roll was represented by a volume-averaged source term. The homogenized jelly-roll domain included the electrode layers and current collectors through their effective material properties, while the electrochemical model supplied the corresponding heat generation. This formulation provided a consistent basis for comparing the thermal responses of the different fin configurations. Its performance was assessed against experimental measurements, as described in Section 2.4.

Table 3. Governing equations and boundary conditions of the P2D electrochemical model [25–27]

		Basic Governing Equations		Boundary Conditions	
Charge conservation	Solid phase	$\frac{\partial}{\partial x}\left(\sigma^{\text{eff}}\frac{\partial \phi_{\text{s}}}{\partial x}\right) = a_{\text{s}} F j^{\text{Li}}$	(1)	$\left.\frac{\partial \phi_{\text{s}}}{\partial x}\right\|_{x=L_{\text{n}}} = 0$	(3)
		$a_{\text{s}} = \frac{3\varepsilon_{\text{s}}}{R_{\text{s}}}$	(2)	$\left.\frac{\partial \phi_{\text{s}}}{\partial x}\right\|_{x=L_{\text{n}}+L_{\text{s}}} = 0$	(4)
				$\left. -\sigma_{\text{n}}^{\text{eff}}\frac{\partial \phi_{\text{s}}}{\partial x}\right\|_{x=0} = i_{\text{app}}$	(5)
				$\left. -\sigma_{\text{p}}^{\text{eff}}\frac{\partial \phi_{\text{s}}}{\partial x}\right\|_{x=L_{\text{n}}+L_{\text{s}}+L_{\text{p}}} = i_{\text{app}}$	(6)
	Electrolyte phase	$\frac{\partial}{\partial x}\left(k^{\text{eff}}\frac{\partial \phi_{\text{e}}}{\partial x}\right) + \frac{\partial}{\partial x}\left(k_{\text{D}}^{\text{eff}}\frac{\partial \ln C_{\text{e}}}{\partial x}\right) = -a_{\text{s}} F j^{\text{Li}}$	(7)	$\left.\frac{\partial \phi_{\text{e}}}{\partial x}\right\|_{x=0} = 0$	(9)
		where, $k_{\text{D}}^{\text{eff}} = \frac{2RT\kappa^{\text{eff}}}{F}(t_{+}^{0}-1)\times\left(1+\frac{\text{d}\ln f_{\pm}}{\text{d}\ln C_{\text{e}}}\right)$	(8)	$\left.\frac{\partial \phi_{\text{e}}}{\partial x}\right\|_{x=L_{\text{n}}+L_{\text{s}}+L_{\text{p}}} = 0$	(10)
Mass conservation	Solid phase	$\frac{\partial C_{\text{s}}}{\partial t} - \frac{D_{\text{s}}}{r^2}\frac{\partial}{\partial r}\left(r^2\frac{\partial C_{\text{s}}}{\partial r}\right) = 0$	(11)	$\left. -D_{\text{s}}\frac{\partial C_{\text{s}}}{\partial r}\right\|_{r=0} = 0$	(12)
				$\left. -D_{\text{s}}\frac{\partial C_{\text{s}}}{\partial r}\right\|_{r=R_{\text{s}}} = j^{\text{Li}}$	(13)
	Electrolyte phase	$\varepsilon_{\text{e}}\frac{\partial C_{\text{e}}}{\partial t} = \frac{\partial}{\partial x}\left(D_{\text{e}}^{\text{eff}}\frac{\partial C_{\text{e}}}{\partial x}\right) + a_{\text{s}}(1-t_{+}^{0})j^{\text{Li}}$	(14)	$\left.\frac{\partial C_{\text{e}}}{\partial x}\right\|_{x=0} = 0$	(15)
				$\left.\frac{\partial C_{\text{e}}}{\partial x}\right\|_{x=L_{\text{n}}+L_{\text{s}}+L_{\text{p}}} = 0$	(16)
Electrochemical kinetics		$j^{\text{Li}} = \frac{i_0}{F}\left[\exp\left(\frac{\alpha_{\text{a}}F}{RT}\eta\right) - \exp\left(-\frac{\alpha_{\text{c}}F}{RT}\eta\right)\right]$			(17)
		where, $\eta = \phi_{\text{s}} - \phi_{\text{e}} - U$			(18)
		$i_0 = k_{\text{m}}(C_{\text{e}})^{\alpha_{\text{a}}}(C_{\text{s,max}} - C_{\text{s,e}})^{\alpha_{\text{a}}}(C_{\text{s,e}})^{\alpha_{\text{c}}}$			(19)
Heat sources		$Q_{\text{gen}} = Q_{\text{rea}} + Q_{\text{ohm}} + Q_{\text{act}}$			(20)
		$Q_{\text{rea}} = F a_{\text{s}} j^{\text{Li}} T\frac{\partial U}{\partial T}$			(21)
		$Q_{\text{ohm}} = \sigma^{\text{eff}}\left(\frac{\partial \phi_{\text{s}}}{\partial x}\right)^2 + k^{\text{eff}}\left(\frac{\partial \phi_{\text{e}}}{\partial x}\right)^2 + \frac{2k^{\text{eff}}RT}{F}(t_{+}^{0}-1)\left[1+\frac{\partial \ln f_{\pm}}{\partial \ln C_{\text{e}}}\right]\frac{\partial \ln C_{\text{e}}}{\partial x}\frac{\partial \phi_{\text{e}}}{\partial x}$			(22)
		$Q_{\text{act}} = F a_{\text{s}} j^{\text{Li}}(\phi_{\text{s}} - \phi_{\text{e}} - U)$			(23)

Note: P2D = pseudo-two-dimensional.

Table 4. Governing equations for three-dimensional heat transfer and airflow [28]

Three-Dimensional Module		Basic Governing Equations	
Solid and fluid heat transfer module		$\rho C_p\frac{\partial T}{\partial t} + \rho C_p\mathbf{u}\cdot\nabla T + \nabla\cdot(-k\nabla T) = Q_{\text{gen}}$	(24)
Laminar flow module	Navier–Stokes equation	$\rho\frac{\partial \mathbf{u}}{\partial t} + \rho(\mathbf{u}\cdot\nabla)\mathbf{u} = \nabla\cdot[-p\mathbf{I}+\mathbf{K}]$	(25)
	Continuity equation	$\nabla\cdot\mathbf{u} = 0$	(26)

2.3 Assessment of Grid and Time Step Independence

Grid and time step independence were assessed using the maximum temperature T_{max} and maximum intra-cell temperature difference ΔT_{max} within the jelly roll as the principal evaluation criteria. These quantities were selected because they directly represent the two thermal performance measures examined in the study: peak operating temperature and internal temperature uniformity.

The selected discretization consisted of 45 elements for the electrochemical model and 46,503 elements for the three-dimensional thermal model. This combination was adopted to provide a suitable balance between numerical accuracy and computational cost.

Temporal discretization was examined using six time steps: 0.1, 0.5, 1, 2, 4, and 6 s. Numerical instability was observed with time steps of 4 and 6 s, whereas stable solutions were obtained with time steps of 2 s or less. Further reductions below 2 s produced no substantial changes in the evaluated temperature quantities. Accordingly, a time step of 2 s was selected for the transient simulations.

2.4 Numerical Method Validation

The coupled electrochemical–thermal model was validated against experimental measurements reported by Akula and Balaji [22] for the Panasonic NCR18650BD cylindrical cell. The experimental measurements were obtained during a 1 C constant-current discharge at an ambient temperature of 24 °C. Cell voltage and mean surface temperature were selected for comparison because they provide complementary measures of electrochemical and thermal behavior during discharge.

The simulated voltage and surface temperature histories were compared with the corresponding experimental measurements, as shown in Figure 4. The simulated voltage and surface temperature followed the corresponding experimental trends throughout discharge, with reported maximum percentage errors of 3.27% and 3.68%, respectively. The agreement between the simulated and experimental results supports the use of the coupled model for evaluating the temperature response of the cylindrical cell under the investigated operating conditions.

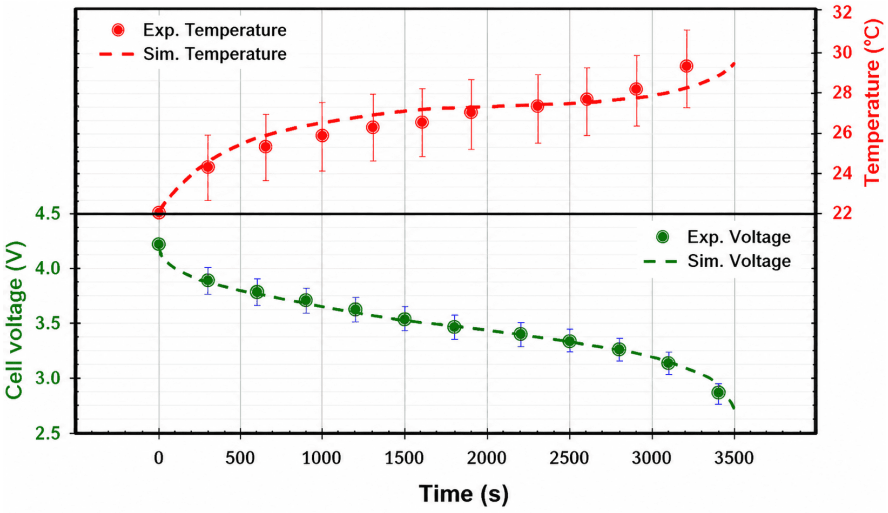


Figure 4. Comparison of simulated and experimental cell voltage and mean surface temperature during 1 C constant-current discharge

Note: Experimental data were obtained from Akula and Balaji [22].

3 Results and Discussion

The thermal performance of the cylindrical LIB was examined using five annular fin configurations with different radius distributions. All fins were made of steel and had a uniform thickness of 2 mm, with radial extensions ranging from 1 to 4 mm, as illustrated in Figure 2. The analysis focused on the maximum cell temperature T_{max} and maximum intra-cell temperature difference ΔT_{max}, which characterize peak thermal conditions and internal temperature uniformity, respectively. Their evolution during discharge is presented in Figure 5, while the corresponding temperature and airflow distributions are shown in Figure 6 and Figure 7.

The finless cell exhibited the highest operating temperature and the greatest internal temperature difference among the investigated configurations. As shown in Figure 5, its maximum temperature exceeded 35 ℃ during discharge. The temperature contours in Figure 6 further show that heat accumulated predominantly in the middle and upper regions of the cell, producing a nonuniform internal temperature distribution. This behavior reflects the

combined effects of internal heat generation, anisotropic heat conduction within the jelly roll, and heat removal through the external surface. In particular, the relatively low radial thermal conductivity restricts heat transfer from the inner regions of the cell toward the cooling air. Consequently, the finless configuration developed a pronounced internal temperature gradient despite the presence of forced airflow.

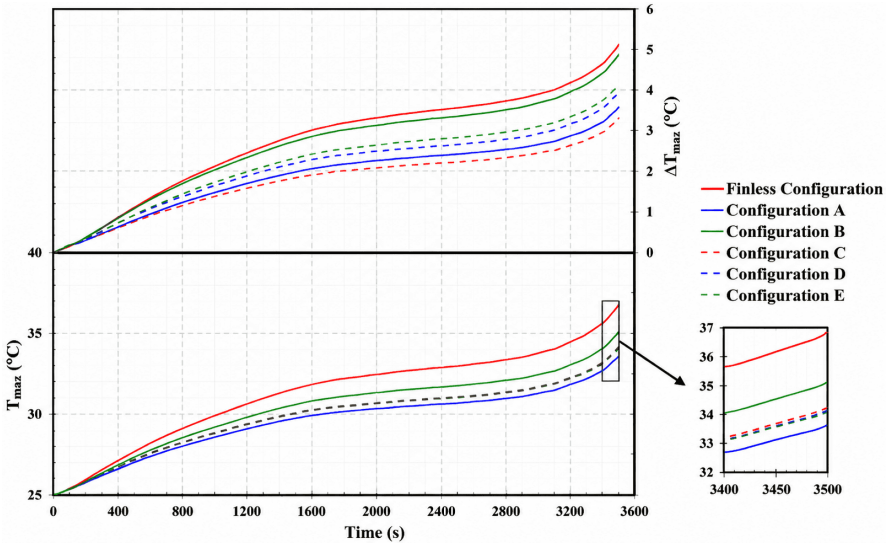


Figure 5. Temporal evolution of the maximum cell temperature T_{max} and maximum intra-cell temperature difference ΔT_{max} for the different fin configurations

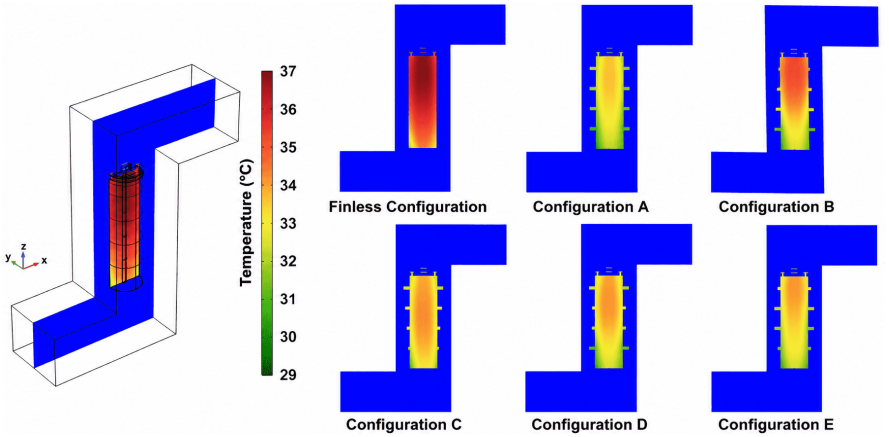


Figure 6. Temperature distributions within the cylindrical battery on the central vertical (X–Z) plane at the end of discharge for the different fin configurations

The addition of annular fins reduced both T_{max} and ΔT_{max} in all five configurations relative to the finless cell (Figure 5). The temperature contours in Figure 6 show a more uniform distribution within the jelly roll, indicating that the fins contributed not only to the removal of heat from the cell surface but also to the reduction of internal temperature gradients. This improvement is particularly relevant to cylindrical batteries, where temperature differences within the active material can influence thermal stresses and long-term operating conditions.

The cooling effect resulted from the combined influence of the additional heat transfer area and the changes in airflow around the battery. The annular fins extended the surface available for convective heat exchange, while their arrangement modified the local velocity field within the cooling channel. As illustrated in Figure 7, regions of higher airflow velocity developed between the finned cell and the surrounding duct walls. The resulting flow redistribution increased convective heat removal from the cell surface and altered the thermal boundary layer. These effects explain the lower temperatures obtained with the finned configurations and demonstrate the importance of fin geometry in determining the thermal response of the battery.

Changes in the airflow field also affected the aerodynamic resistance of the cooling channel. The pressure drop was 0.194 Pa for the finless configuration and increased to 0.265, 0.235, 0.226, 0.253, and 0.231 Pa for Configurations A, B, C, D, and E, respectively. The additional resistance arose from the interaction between the airflow and the

fin surfaces, which modified the available flow passages and local velocity distribution. Among the finned designs, Configuration A produced the highest pressure drop (0.265 Pa), whereas Configuration C produced the lowest (0.226 Pa). These results show that the arrangement of annular fins influences both heat removal and the pressure required to maintain airflow through the cooling channel. Fin radius distribution is therefore an important design parameter when thermal performance and aerodynamic resistance are considered together.

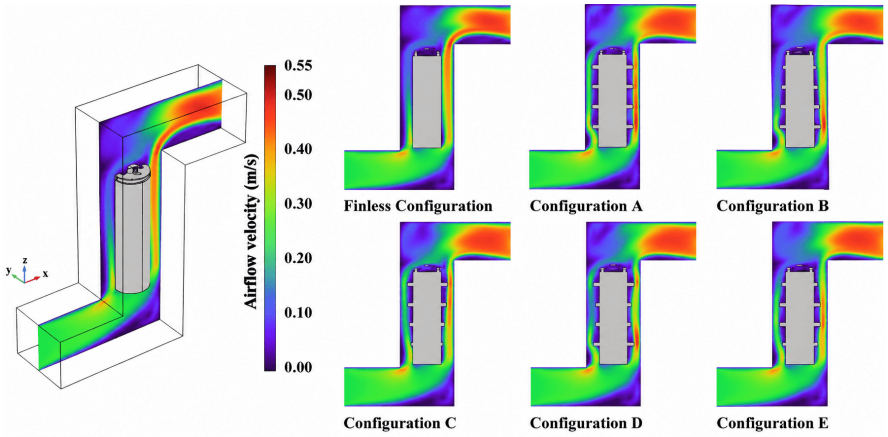


Figure 7. Airflow velocity distributions on the central vertical (X–Z) plane at the end of discharge for the different fin configurations

Note: The battery and fins are shown in grey.

Configuration A, consisting of four annular fins with a uniform radial extension of 4 mm, achieved the lowest T_{max} among the investigated designs. Its larger heat transfer area provided greater contact with the cooling air, while the velocity contours in Figure 7 indicate stronger local airflow near the finned surface. The combination of these effects increased heat removal and produced the greatest reduction in peak cell temperature. However, the larger fins also required more material and generated a pressure drop of 0.265 Pa, the highest value among the five finned configurations. More importantly, Configuration A did not produce the lowest ΔT_{max}. This distinction shows that minimizing the maximum cell temperature and improving temperature uniformity within the cell are related but separate thermal management objectives.

Configuration C, which employed annular fins with increasing radii along the airflow direction, produced the lowest ΔT_{max} among the configurations examined. Its average maximum intra-cell temperature difference was 5.8% lower than that of Configuration A. At the same time, Configuration C required 37.5% less fin material and reduced the pressure drop by approximately 15% relative to Configuration A, from 0.265 to 0.226 Pa. The reduction in internal temperature difference indicates that the increasing-radius arrangement provided a more favorable distribution of cooling along the cell, even though Configuration A achieved the lowest peak temperature. By varying the fin dimensions rather than maintaining the maximum radial extension at every position, Configuration C achieved a more uniform internal thermal response with lower material consumption and airflow resistance.

The comparison between Configurations A and C highlights the importance of distinguishing peak temperature reduction from internal temperature uniformity when designing air-cooled BTMSs. Configuration A was most effective in reducing T_{max}, whereas Configuration C provided the most favorable combination of internal temperature uniformity, fin material use, and pressure drop. The results establish that increasing the fin surface area uniformly is not necessarily the most effective approach when internal temperature differences are the primary design criterion. Instead, distributing the cooling surface along the cell offers a means of controlling the spatial temperature field while limiting material requirements and aerodynamic resistance. For cylindrical LIBs used in EVs and related energy storage systems, the increasing-radius annular fin arrangement provides a practical design option for improving internal thermal uniformity under the investigated operating conditions.

4 Conclusions

This study investigated the effects of uniform- and variable-radius annular cooling fins on the thermal performance and internal temperature uniformity of a cylindrical LIB. A three-dimensional transient electrochemical–thermal model, coupled with a one-dimensional P2D electrochemical model, was developed in COMSOL Multiphysics 6.2. Five annular fin configurations were compared with a finless design in a Z-shaped air-cooling channel at an inlet velocity of 0.25 m/s and an air temperature of 25 °C. The analysis focused on the maximum cell temperature, maximum intra-cell temperature difference, and airflow resistance.

All fin configurations reduced the maximum cell temperature and internal temperature difference relative to the

finless design, for which the maximum temperature exceeded 35 °C. The uniform-radius configuration (Configuration A) achieved the lowest maximum temperature through its larger heat transfer area and increased local airflow velocity. However, it also produced the highest pressure drop and required the greatest amount of fin material. In contrast, the increasing-radius configuration (Configuration C) achieved the most uniform internal temperature distribution. Compared with Configuration A, it reduced the average maximum intra-cell temperature difference by 5.8%, fin material consumption by 37.5%, and pressure drop by approximately 15%. These results demonstrate that the spatial distribution of annular fin radii is an important design parameter for controlling internal temperature gradients while reducing material requirements and aerodynamic resistance.

The results show that maximum temperature reduction and internal temperature uniformity should be considered separately when designing air-cooled cylindrical battery systems. Rather than relying solely on a larger cooling surface, the increasing-radius arrangement provided a more favorable balance between temperature uniformity, material use, and pressure drop under the investigated operating conditions. This finding provides a practical basis for the design of annular fin arrangements in BTMSs for EVs and related energy storage applications. Future work can extend the analysis to multi-cell battery modules and examine the effects of discharge rate, inlet airflow velocity, and cooling air temperature on the performance of variable-radius annular fins.

Author Contributions

Conceptualization, G.L.; methodology, G.L.; formal analysis, G.L.; investigation, R.F., L.C., P.V., R.S., D.P.-V., and S.P.; data curation, R.F., L.C., P.V., R.S., D.P.-V., and S.P.; writing—original draft preparation, R.F., L.C., P.V., R.S., D.P.-V., and S.P.; writing—review and editing, G.L.; visualization, G.L.; supervision, G.L. All authors have read and agreed to the published version of the manuscript.

Funding

This work is funded by Ministero dell'Università e della Ricerca and Unione Europea–NextGenerationEU (Grant No.: 2022BTSF52).

Data Availability

The data used to support the research findings are available from the corresponding author upon request.

Conflicts of Interest

The authors declare no conflicts of interest.

References

[1] A. Verma, A. Prajapati, and D. Rakshit, "A comparative study on prismatic and cylindrical lithium-ion batteries based on their performance in high ambient environment," *J. Inst. Eng. India Ser. C*, vol. 103, pp. 149–166, 2022. https://doi.org/10.1007/s40032-021-00760-1

[2] H. Sharma, G. Saxena, R. S. Rajput, and R. Randa, "Optimization of process parameters of novel hybrid automotive battery cooling system using GRA-Taguchi and heatmap visualization," *J. Inst. Eng. India Ser. C*, vol. 106, pp. 1281–1303, 2025. https://doi.org/10.1007/s40032-025-01204-w

[3] L. Mattia, H. Beiranvand, W. Zamboni, and M. Liserre, "Lithium-ion battery thermal modelling and characterisation: A comprehensive review," *J. Energy Storage*, vol. 129, p. 117114, 2025. https://doi.org/10.1016/j.est.2025.117114

[4] X. Gu, W. Lei, J. Xi, and M. Song, "Investigation and optimization of battery thermal management system based on composite phase change material and variable wall liquid cooling plate," *Int. J. Thermofluids*, vol. 24, p. 100886, 2024. https://doi.org/10.1016/j.ijft.2024.100886

[5] Z. Sun, Y. Guo, C. Zhang, J. Whitehouse, Q. Zhou, H. Xu, and C. Wang, "Experimental study of battery passive thermal management system using copper foam-based phase change materials," *Int. J. Thermofluids*, vol. 17, p. 100255, 2023. https://doi.org/10.1016/j.ijft.2022.100255

[6] H. Khoharo, J. Selvaraj, M. Hasanuzzaman, L. Kumar, and R. Manghwar, "Global advancement, prospect and challenges of battery thermal management systems: A comprehensive review," *Renew. Sustain. Energy Rev.*, vol. 222, p. 115923, 2025. https://doi.org/10.1016/j.rser.2025.115923

[7] Y. S. Choi and D. M. Kang, "Prediction of thermal behaviors of an air-cooled lithium-ion battery system for hybrid electric vehicles," *J. Power Sources*, vol. 270, pp. 273–280, 2014. https://doi.org/10.1016/j.jpowsour.2014.07.120

[8] A. S. Soliman and P. Cheng, "A comprehensive review of battery thermal management systems: Enhancing performance, thermal models, and economic analysis," *J. Energy Storage*, vol. 153, p. 120880, 2026. https://doi.org/10.1016/j.est.2026.120880

[9] A. Alzwayi and M. C. Paul, "Effective battery pack cooling by controlling flow patterns with vertical and spiral fins," *Therm. Sci. Eng. Prog.*, vol. 55, p. 102907, 2024. https://doi.org/10.1016/j.tsep.2024.102907

[10] B. A. Osaimi and H. M. Ali, "Review of thermal management strategies for cylindrical lithium-ion batteries: Active, passive, and hybrid approaches," *Energy Rep.*, vol. 15, p. 108915, 2026. https://doi.org/10.1016/j.egyr.2025.12.052

[11] Q. Wang, B. Jiang, B. Li, and Y. Yan, "A critical review of thermal management models and solutions of lithium-ion batteries for the development of pure electric vehicles," *Renew. Sustain. Energy Rev.*, vol. 64, pp. 106–128, 2016. https://doi.org/10.1016/j.rser.2016.05.033

[12] M. G. Kibria, M. S. Mohtasim, U. K. Paul, I. A. Fahim, Nafi, B. K. Das, and H. A. Mohammed, "A review on composite phase change materials and fins-based Li-ion battery thermal management systems with design perspectives and future outlooks," *Energy Fuels*, vol. 38, no. 15, pp. 13 637–13 660, 2024. https://doi.org/10.1021/acs.energyfuels.4c02062

[13] M. Öztop and A. Şahinaslan, "Control of temperature distribution for Li-ion battery modules via longitudinal fins," *J. Energy Storage*, vol. 52, p. 104760, 2022. https://doi.org/10.1016/j.est.2022.104760

[14] S. M. Shehabaz, S. K. Gugulothu, R. Muthyala, P. Vishnu, P. Buliraju, and G. Sailaja, "Numerical characterization and optimization of hybrid battery thermal management system integrating with nano-PCM and passive and active cooling synergies under variable discharge rates," *J. Therm. Sci. Eng. Appl.*, vol. 18, no. 1, p. 011003, 2026. https://doi.org/10.1115/1.4069841

[15] J. Alfred Francis, M. Surya, and D. Rajagopal, "Numerical analysis of spiral fins on thermal management of a lithium-ion battery," *Results Eng.*, vol. 31, p. 111606, 2026. https://doi.org/10.1016/j.rineng.2026.111606

[16] A. S. Alzwayi and M. C. Paul, "Heat transfer enhancement of a lithium-ion battery cell using vertical and spiral cooling fins," *Therm. Sci. Eng. Prog.*, vol. 47, p. 102304, 2024. https://doi.org/10.1016/j.tsep.2023.102304

[17] J. Chaudhari, G. K. Singh, M. K. Rathod, and H. M. Ali, "Experimental and computational analysis on lithium-ion battery thermal management system utilizing air cooling with radial fins," *J. Therm. Anal. Calorim.*, vol. 149, pp. 203–218, 2024. https://doi.org/10.1007/s10973-023-12698-w

[18] P. Han, J. Wang, X. Zhao, J. Liu, C. Wang, and X. She, "Performance study of fin structure in air-cooled thermal management system for column power battery," *J. Energy Storage*, vol. 104, p. 114697, 2024. https://doi.org/10.1016/j.est.2024.114697

[19] A. A. Omar and A. M. Adham, "Thermal analysis of lithium-ion batteries using forced-air cooling and circular fin systems: A numerical study," *Int. J. Thermofluids*, vol. 27, p. 101212, 2025. https://doi.org/10.1016/j.ijft.2025.101212

[20] A. B. Koucheh, P. Sharbati, C. Ünlü, A. Koşar, and A. Sadaghiani, "Comprehensive evaluation of battery cooling mechanisms including two-phase immersion with 3M NOVEC-7000 and 7100," *Energy Convers. Manage.*, vol. 348, p. 120780, 2025. https://doi.org/10.1016/j.enconman.2025.120780

[21] Panasonic, "Specifications for NCR18650BD," 2026. https://www.evwest.com/support/panasonic-ncr18650bd-datasheet.pdf

[22] R. Akula and C. Balaji, "Thermal management of 18650 Li-ion battery using novel fins–PCM–EG composite heat sinks," *Appl. Energy*, vol. 316, p. 119048, 2022. https://doi.org/10.1016/j.apenergy.2022.119048

[23] H. Yu, X. Zhu, X. Ma, and H. Yan, "Cooling performance analysis and sensitivity analysis of thermoelectric cooling for an 18650 battery pack thermal management," *Case Stud. Therm. Eng.*, vol. 72, p. 106394, 2025. https://doi.org/10.1016/j.csite.2025.106394

[24] M. Doyle, T. F. Fuller, and J. Newman, "Modeling of galvanostatic charge and discharge of the lithium/polymer/insertion cell," *J. Electrochem. Soc.*, vol. 140, no. 6, pp. 1526–1533, 1993. https://doi.org/10.1149/1.2221597

[25] Y. Ye, Y. Shi, N. Cai, J. Lee, and X. He, "Electro-thermal modeling and experimental validation for lithium ion battery," *J. Power Sources*, vol. 199, pp. 227–238, 2012. https://doi.org/10.1016/j.jpowsour.2011.10.027

[26] X. W. Lin, Z. F. Zhou, X. G. Zhu, B. Chen, H. Zhu, N. Y. Ben, X. D. Wang, and W. W. Xu, "Non-uniform thermal characteristics investigation of three-dimensional electrochemical-thermal coupled model for pouch lithium-ion battery," *J. Cleaner Prod.*, vol. 417, p. 137912, 2023. https://doi.org/10.1016/j.jclepro.2023.137912

[27] G. Liu and L. Zhang, "Research on the thermal characteristics of an 18650 lithium-ion battery based on an electrochemical–thermal flow coupling model," *World Electr. Veh. J.*, vol. 12, no. 4, p. 250, 2021. https://doi.org/10.3390/wevj12040250

[28] Y. Du, M. Xu, K. Jiao, C. Ma, and D. Deng, "Simulation model of temperature field for ultra-thin overlay construction based on fluid-solid coupling heat transfer," *Appl. Therm. Eng.*, vol. 289, p. 129849, 2026. https://doi.org/10.1016/j.applthermaleng.2026.129849

[29] T. R. Ashwin, A. McGordon, W. D. Widanage, and P. A. Jennings, "Modified electrochemical parameter estimation of NCR18650BD battery using implicit finite volume method," *J. Power Sources*, vol. 341, pp.

387–395, 2017. https://doi.org/10.1016/j.jpowsour.2016.12.023

[30] J. Sturm, A. Rheinfeld, I. Zilberman, F. B. Spingler, S. Kosch, F. Frie, and A. Jossen, "Modeling and simulation of inhomogeneities in a 18650 nickel-rich, silicon-graphite lithium-ion cell during fast charging," *J. Power Sources*, vol. 412, pp. 204–223, 2019. https://doi.org/10.1016/j.jpowsour.2018.11.043

Appendix

Table A1. The values of parameters used in the electrochemical model [22, 27–30]

Notation	Parameters Name	Unit	Value Positive Electrode	Negative Electrode	Separator
σ^{eff}	Effective solid-phase electronic conductivity	$\mathrm{S/m}$	3.8	100	—
ε_{s}	Solid-phase volume fraction	—	0.44	0.4	1
R_{s}	Particle radius	m	8×10^{-6}	12.5×10^{-6}	—
L	Thickness	m	138×10^{-6}	149×10^{-6}	32×10^{-6}
C_{e}	Initial lithium concentration in electrolyte phase	$\mathrm{mol/m^3}$	2000	2000	2000
C_{s}	Maximum lithium concentration in solid phase	$\mathrm{mol/m^3}$	48,000	31,507	—
t_+^0	Li^+ transference number	—	0.363	0.363	0.363
$f^{\pm}$	Electrolyte activity coefficient	—	1	1	1
D_{s}	Solid-phase diffusion coefficient	$\mathrm{m^2/s}$	1.5×10^{-15}	3.9×10^{-14}	—
ε_{e}	Electrolyte phase volume fraction	—	0.3	0.3	0.5
$D_{\text{e}}^{\text{eff}}$	Electrolyte phase diffusion coefficient	$\mathrm{m^2/s}$	2.6×10^{-6}	2.6×10^{-6}	2.6×10^{-6}
α_{a}	Anodic-transfer coefficient	—	0.5	0.5	—
α_{c}	Cathodic-transfer coefficient	—	0.5	0.5	—
k_{m}	Reaction rate constant	$\mathrm{m^{2.5}/(mol^{0.5} \cdot s)}$	2.072×10^{-11}	2.072×10^{-11}	—
F	Faraday's constant	$\mathrm{C/mol}$		9.6485×10^4	
R	Gas constant	$\mathrm{J/(mol \cdot K)}$		8.314	

Note: "—" = not applicable.